

Competing spin-orbital singlet states in the $4d^4$ honeycomb ruthenate $\text{Ag}_3\text{LiRu}_2\text{O}_6$

T. Takayama^{1,2,*}, M. Blankenhorn,^{1,2} J. Bertinshaw,¹ D. Haskel³, N. A. Bogdanov⁴, K. Kitagawa,⁴ A. N. Yaresko,¹ A. Krajewska,^{1,2,5} S. Bette,¹ G. McNally,¹ A. S. Gibbs,^{5,6} Y. Matsumoto,¹ D. P. Sari^{7,8}, I. Watanabe⁸, G. Fabbris,³ W. Bi,^{3,9} T. I. Larkin,¹ K. S. Rabinovich,¹ A. V. Boris,¹ H. Ishii,¹⁰ H. Yamaoka¹¹, T. Irifune,¹² R. Bewley,⁵ C. J. Ridley,⁵ C. L. Bull^{5,13}, R. Dinnebier,¹ B. Keimer,¹ and H. Takagi^{1,2,4}

¹Max Planck Institute for Solid State Research, Heisenbergstrasse 1, 70569 Stuttgart, Germany

²Institute for Functional Matter and Quantum Technologies, University of Stuttgart, Pfaffenwaldring 57, 70550 Stuttgart, Germany

³Advanced Photon Source, Argonne National Laboratory, Argonne, Illinois 60439, USA

⁴Department of Physics, University of Tokyo, 7-3-1 Hongo, Bunkyo-ku, Tokyo 113-0033, Japan

⁵ISIS Neutron and Muon Source, STFC Rutherford Appleton Laboratory, Chilton, Didcot, Oxon OX11 0QX, United Kingdom

⁶School of Chemistry, University of St Andrews, St Andrews, KY16 9ST, United Kingdom

⁷Innovative Global Program, College of Engineering, Shibaura Institute of Technology, Saitama 337-8570, Japan

⁸Meson Science Laboratory, RIKEN Nishina Center for Accelerator-Based Science, Wako, Saitama 351-0198, Japan


⁹Department of Physics, University of Alabama at Birmingham, Birmingham, Alabama 35294, USA

¹⁰National Synchrotron Radiation Research Center, Hsinchu 30076, Taiwan

¹¹RIKEN SPring-8 Center, Sayo, Hyogo 679-5148, Japan

¹²Geodynamics Research Center, Ehime University, Matsuyama, 790-8577, Japan

¹³School of Chemistry, University of Edinburgh, David Brewster Road, Edinburgh EH9 3FJ, United Kingdom

 (Received 5 March 2022; revised 10 September 2022; accepted 5 October 2022; published 7 November 2022)

When spin-orbit-entangled d electrons reside on a honeycomb lattice, rich quantum states are anticipated to emerge, as exemplified by the d^5 Kitaev materials. Distinct yet equally intriguing physics may be realized with a d -electron count other than d^5 . The magnetization, ^7Li -nuclear magnetic resonance (NMR), and inelastic neutron scattering measurements, together with the quantum chemistry calculation, indicate that the layered ruthenate $\text{Ag}_3\text{LiRu}_2\text{O}_6$ with d^4 Ru^{4+} ions at ambient pressure forms a honeycomb lattice of spin-orbit-entangled singlets, which is a playground for frustrated excitonic magnetism. Under pressure, the singlet state does not develop the expected excitonic magnetism, but two successive transitions to other nonmagnetic phases were found in ^7Li -NMR, neutron diffraction, and x-ray absorption fine structure measurements, first to an intermediate phase with moderate distortion of honeycomb lattice and eventually to a high-pressure phase with very short Ru-Ru dimer bonds. While the strong dimerization in the high-pressure phase originates from a molecular orbital formation as in the sister compound Li_2RuO_3 , we argue that the intermediate phase represents a spin-orbit-coupled singlet dimer state which is stabilized by the admixture of upper-lying $J_{\text{eff}} = 1$ -derived states via a pseudo-Jahn-Teller effect. The emergence of competing electronic phases demonstrates rich spin-orbital physics of d^4 honeycomb compounds, and this finding paves the way for realization of unconventional magnetism.

DOI: [10.1103/PhysRevResearch.4.043079](https://doi.org/10.1103/PhysRevResearch.4.043079)

I. INTRODUCTION

The interplay of electron correlation and spin-orbit coupling (SOC) in $4d$ and $5d$ transition-metal compounds has been recognized as a key ingredient in realizing unprecedented electronic phases. The energy scale of SOC for $4d$ and $5d$ transition-metal ions is comparable with the other relevant electronic parameters such as Hund's coupling, intersite hop-

ping, and the noncubic crystal field in those systems, giving rise to the formation of a spin-orbit-entangled wave function [1,2]. Magnetic couplings between spin-orbit-entangled moments are often anisotropic, reflecting the inherited orbital degree of freedom, which is distinct from those of spin-only magnetic moments and realizes rich and exotic magnetic ground states [2,3]. Serving as prime examples are compounds with a honeycomb lattice of spin-orbit-entangled moments. Those with d^5 and d^1 ions are proposed theoretically to host a class of quantum liquids, the Kitaev spin liquid [4,5] and a $\text{SU}(4)$ spin-orbital liquid [6], respectively, and the experimental realization for such quantum liquid states has been intensively pursued.

Honeycomb-lattice compounds with d^4 transition-metal ions, which are coordinated octahedrally with ligand anions, are another playground for exotic magnetism. All four d electrons are accommodated in the low-lying t_{2g} manifold because

*t.takayama@fkf.mpg.de

Published by the American Physical Society under the terms of the [Creative Commons Attribution 4.0 International license](https://creativecommons.org/licenses/by/4.0/). Further distribution of this work must maintain attribution to the author(s) and the published article's title, journal citation, and DOI. Open access publication funded by the Max Planck Society.

of the large cubic crystal field for $4d$ and $5d$ transition-metal ions. Hund's coupling leads to the formation of spin moment $S = 1$ and effective orbital moment $L_{\text{eff}} = 1$ in the LS -coupling scheme. SOC splits $S = 1$, $L_{\text{eff}} = 1$ manifold into spin-orbit-entangled $J_{\text{eff}} = 0, 1$, and 2 states. The ground state for an isolated ion is the nonmagnetic $J_{\text{eff}} = 0$ singlet [1]. It is proposed theoretically that a $J_{\text{eff}} = 0$ Mott insulator experiences a quantum phase transition to a magnetically ordered state when the exchange interactions through the upper-lying $J_{\text{eff}} = 1$ state overcome the excitation gap from the $J_{\text{eff}} = 0$ to 1 states [7,8]. This magnetic transition can be viewed as condensation of $J_{\text{eff}} = 1$ triplet excitons and is dubbed excitonic magnetism. The antiferromagnetically ordered state of the layered perovskite Ca_2RuO_4 was recently shown to be a realization of such excitonic magnetism, and a Higgs-mode excitation was identified in the spin-wave dispersion measured by inelastic neutron scattering (INS) and in Raman spectra [9,10].

The excitonic magnetism of Ca_2RuO_4 with corner-shared RuO_6 octahedra is produced predominantly by Heisenberg-type exchange interactions through the excited $J_{\text{eff}} = 1$ states in the nearly 180° Ru-O-Ru bonds. In the network of edge-shared octahedra with 90° bonding geometry, the exchange interaction via the $J_{\text{eff}} = 1$ triplet is dependent on the dominant hopping process and anisotropic in contrast to the corner-shared case. The anisotropic coupling brings about a frustration in developing excitonic magnetism, especially on a honeycomb lattice. When the hopping via anion p -orbitals, d - p - d hopping, is dominant in the 90° bond, the exchange interaction takes the form of bond-dependent XY-interactions. Magnetic correlations in such a case develop only along the one-dimensional zigzag chain segments of honeycomb lattice, which is predicted to give rise to a spin-nematic state [7]. If the direct d - d hopping across the edges is dominant, a bond-dependent Ising interaction of the Kitaev type is proposed to appear [11,12]. Strong frustration originating from the Kitaev-type interaction is expected to suppress the long-range magnetic ordering and lead to a $J_{\text{eff}} = 1$ triplon liquid phase, which is regarded as a bosonic analog of the Kitaev honeycomb model. When both hopping processes contribute with comparable magnitudes, condensation of the $J_{\text{eff}} = 1$ triplet, namely, long-range magnetic ordering with soft moments, takes place as in Ca_2RuO_4 [12]. With introducing the lattice degree of freedom, an even richer variety of spin-orbit-entangled phases may emerge. The d^4 honeycomb systems are therefore a promising playground to explore such exotic magnetic ground states.

There are d^4 honeycomb materials which are nonmagnetic. They, however, do not represent a good starting point to explore the expected exotic magnetism. The $5d^4$ honeycomb iridate NaIrO_3 , a Na-deficient analog of Na_2IrO_3 , displays almost temperature-independent magnetic susceptibility [13]. The nonmagnetic insulating state implies that NaIrO_3 is viewed as a $J_{\text{eff}} = 0$ Mott insulator if the LS -coupling scheme is justified. The large SOC-induced gap of 0.4 eV to the $J_{\text{eff}} = 1$ triplet in $5d^4$ iridates [14], however, is hard to reach by softening due to the exchange interactions, placing it far away from the excitonic magnetism. Additionally, the large SOC is comparable with Hund's coupling, and a jj -coupling character is nonnegligible in NaIrO_3 . The $4d^4$ honeycomb systems

with a moderate SOC should be more suitable for realizing excitonic and related magnetisms. The well-known $4d^4$ honeycomb ruthenate Li_2RuO_3 , however, experiences a strong Ru-Ru dimerization $< \sim 540$ K accompanied by a formation of molecular orbitals (MOs) [15,16]. In the dimerized state, the spin and orbital degrees of freedom are fully quenched, hampering the formation of a spin-orbit-entangled state.

To realize the $J_{\text{eff}} = 0$ state on a honeycomb lattice, strong Ru-Ru dimerization needs to be evaded. We utilized a soft-chemical reaction to suppress the Ru-Ru dimerization of Li_2RuO_3 . The silver-intercalated Li_2RuO_3 , $\text{Ag}_3\text{LiRu}_2\text{O}_6$, shows no dimerization down to the lowest temperature measured at ambient pressure [17,18]. The magnetic and spectroscopic measurements, together with the quantum chemistry calculation, indicate that $\text{Ag}_3\text{LiRu}_2\text{O}_6$ is a Mott insulator and hosts a spin-orbit-entangled singlet state derived from $J_{\text{eff}} = 0$ (J singlet). With the application of pressure, $\text{Ag}_3\text{LiRu}_2\text{O}_6$ exhibits two successive phase transitions from the J -singlet state to other nonmagnetic phases, accompanied by structural distortions. The structure of the higher-pressure phase comprises very short Ru-Ru bonds as in Li_2RuO_3 , indicating the strong Ru-Ru dimerization and hence a molecular-orbital formation. The intermediate phase in contrast experiences only a modest distortion of the honeycomb lattice. We propose that the intermediate phase hosts SOC weak dimers where the lattice distortion leads to admixture of $J_{\text{eff}} = 1$ -derived states into the singlet state and lowers its energy. The lattice distortion may be viewed as a pseudo-Jahn-Teller (JT) effect associated with low-lying spin-orbital excitations, which is potentially inherent in d^4 honeycomb compounds. The emergence of competing spin-orbital phases points to the intricate interplay between SOC, exchange interactions, and the lattice in the honeycomb lattice of d^4 ions, and the understanding of the phase competition should give a clue to realize exotic magnetic ground states.

II. EXPERIMENTAL AND THEORETICAL METHODS

Polycrystalline samples of $\text{Ag}_3\text{LiRu}_2\text{O}_6$ were synthesized by an ion-exchange reaction [17]. Powder of Li_2RuO_3 was synthesized from stoichiometric mixture of Li_2CO_3 and RuO_2 . The mixture was pelletized and heated at 1000°C for 48 h with an intermediate grinding. The obtained Li_2RuO_3 powder was mixed with $10\times$ excess of AgNO_3 , and the mixture was heated at 240°C for 72 h in air and slowly cooled to room temperature. The product was rinsed with distilled water to remove remaining AgNO_3 and a side-product of LiNO_3 and dried at room temperature. For the neutron experiments, the ^7Li -enriched precursor $^7\text{Li}_2\text{RuO}_3$ was prepared by using $^7\text{Li}_2\text{CO}_3$, and the ion-exchange reaction was conducted on it.

The obtained samples were characterized by powder x-ray diffraction [19]. The magnetization, transport, and thermodynamic properties were evaluated by using commercial instruments (Quantum Design MPMS3 and PPMS). Spectroscopic ellipsometry was used to determine the dielectric function of $\text{Ag}_3\text{LiRu}_2\text{O}_6$ in the wide spectral range from 10 meV to 6.5 eV at temperatures from 7 to 300 K. A cold-pressed pellet was used for the optical measurement.

The nuclear magnetic resonance (NMR) experiment was carried out using a coherent pulsed spectrometer and a

cryo-cooled preamplifier. The frequency-swept spectra were acquired using a Fourier-step-sum technique, where each Fourier-transformed spectrum shifted with its center frequency was accumulated. The spin-lattice relaxation time T_1 for ^7Li nuclei was measured by a comb-shaped pulse recovery method with an empirical stretched-exponential recovery function $1 - \exp\{-(t/T_1)^\beta\}$. For $T > 100$ K, where the intrinsic gapped behavior is observed, typical values of the stretch exponent β are 0.9–1.0. Here, β decreases and approaches 0.5 as T is lowered because $1/T_1$ is highly influenced by the spin defects.

The muon spin relaxation (μSR) measurements were conducted with double-pulsed muon beam on CHRONUS and ARGUS spectrometers at the RIKEN-RAL muon facilities. The measurement at ambient pressure was conducted on CHRONUS for zero-field and longitudinal-field (LF) conditions. The experiment under hydrostatic pressure was performed on ARGUS using Cu-Be cylinder pressure cell. All collected data were analyzed by using WIMDA software [20].

The time-of-flight INS study was carried out using the thermal spectrometer MAPS at the ISIS Neutron and Muon Source. A 5 g polycrystalline sample of isotope-enriched $\text{Ag}_3^7\text{LiRu}_2\text{O}_6$ was used for the experiment. Measurements were conducted with an incident energy $E_i = 100$ meV and chopper frequency of 400 Hz, giving a calculated energy resolution $\Delta E \sim 3$ meV in the energy transfer range studied. In this configuration, the collection time for each measurement was 4 h.

Magnetization data under hydrostatic pressure were collected using an opposed-anvil-type pressure cell [21]. The pressure cell is made of nonmagnetic Cu-Be alloy, and $\text{ZrO}_2\text{-Al}_2\text{O}_3$ composite ceramic anvils were used. The polycrystalline pellet of $\text{Ag}_3\text{LiRu}_2\text{O}_6$ was placed in a hole of a Cu-Be gasket, together with a small piece of Pb as a pressure marker. Daphne 7474 oil was used as a pressure-transmitting medium.

The resistivity measurements up to 6.2 GPa were performed with a conventional four-probe method using an opposed-anvil-type pressure cell [22]. Daphne 7474 oil was used as a pressure medium, and pressure was measured by the fluorescence spectra of a ruby ball. The NMR measurements under hydrostatic pressure were performed by using an opposed-anvil-type pressure cell [22]. Daphne 7575 was used as pressure transmitting medium, and pressure was determined by ruby R_1 fluorescence scale just after cell clamp.

The powder neutron diffraction data under hydrostatic pressure were collected at the PEARL instrument at the ISIS Neutron and Muon Source [23]. Pressure was applied by using a Paris-Edinburgh press up to 5.2 GPa [24]. The anvils were single-toroidal zirconia-toughened alumina, and an encapsulated TiZr gasket was used. Deuterium substituted methanol-ethanol mixture (4:1 by volume) was used as a hydrostatic pressure medium. The measurements were performed at room temperature, 200, and 120 K.

The powder x-ray diffraction measurements under pressure were performed at BL12B2 of SPring-8. The pressure was applied by using a diamond anvil cell (DAC; Almax easyLab). The wavelength of the x ray was 0.6857 Å. All data were collected at room temperature.

X-ray absorption fine structure (XAFS) measurements at the Ru K -edge under pressure were carried out at beamline 4-ID-D of the Advanced Photon Source at Argonne National Laboratory. A copper-beryllium DAC fitted with compression and decompression He gas membranes for *in situ* pressure control was mounted in a variable temperature insert of a He vapor cryostat. The DAC was fitted with nanopolycrystalline diamond (NPD) anvils with 400 μm diameter culet size [25]. The NPD anvils allow collection of high-quality XAFS data without contamination by strong diamond Bragg peaks typical of single-crystalline anvils [26]. A 200 μm diameter hole drilled in a stainless steel gasket pre-indented to 52 μm thickness was used as the sample chamber. Sample powder was mixed with silicon oil as the pressure medium and loaded into the chamber together with ruby spheres used for *in situ* pressure calibration using an online ruby fluorescence system. Pressure was measured before and after data collection leading to pressure uncertainty estimates of 0.05 (0.2) GPa for data below (above) 2 GPa. XAFS data were collected in transmission geometry using N_2 (Ar)-filled gas ionization chambers as detectors of incident (transmitted) intensity, respectively.

The electronic structure of $\text{Ag}_3\text{LiRu}_2\text{O}_6$ at ambient pressure was studied by embedded cluster quantum chemistry calculations. The calculations were performed with the complete-active-space-self-consistent-field (CASSCF) [27] and the multireference configuration-interaction (MRCI) methods [28]. The energies of low-lying local states of Ru^{4+} were computed using a 37-site $[\text{Ru}_4\text{O}_{18} \text{Li}_3\text{Ag}_{12}]^{5-}$ cluster, which contains one central RuO_6 octahedron, three neighboring RuO_6 octahedra, and the nearby Li and Ag ions. The solid-state surrounding was modeled by the crystal Madelung field within the cluster region, as obtained by the Ewald summation for the periodic system assuming formal ionic charges and represented by a large array of fitted point charges. To obtain a clear picture on crystal-field effects and spin-orbit interactions at the central Ru site, we replaced the neighboring Ru^{4+} ions with diamagnetic Pd^{4+} species. This is a usual procedure in quantum chemistry studies on transition-metal systems, see, for example, Refs. [29,30]. We used an energy-consistent relativistic pseudopotential together with $5s5p4d2f$ and $4s4p3d$ valence basis sets for the central and neighboring Ru ions, respectively [31]. For the six adjacent ligands, we employed an all-electron basis with $4s3p2d$ functions from the cc-pVTZ basis set [32] along with the minimal $2s1p$ atomic-natural-orbital basis set [33] for the O coordinating neighboring Ru sites but not shared with the central octahedron. The Li and Ag species were modeled by monovalent total-ion effective potentials supplemented with a single s function [34,35]. All O $2s2p$ and Ru $4d$ electrons at the central octahedron were correlated in the MRCI calculations [28]. The latter are performed with single and double substitutions with respect to CASSCF(4e, 5o), which is referred to as MRCISD. In CASSCF(4e, 5o) [27] calculations, four active electrons correlated in five Ru $4d$ orbitals. Orbitals were optimized for the average of the lowest three triplet, six singlet, and two quintet states. To separate valence orbitals into the central-octahedron and adjacent-octahedra groups, we used the Pipek-Mezey localization [36]. The effect of SOC was considered using the state interaction formalism within the lowest three triplets, six singlets, and two quintets [37] at both

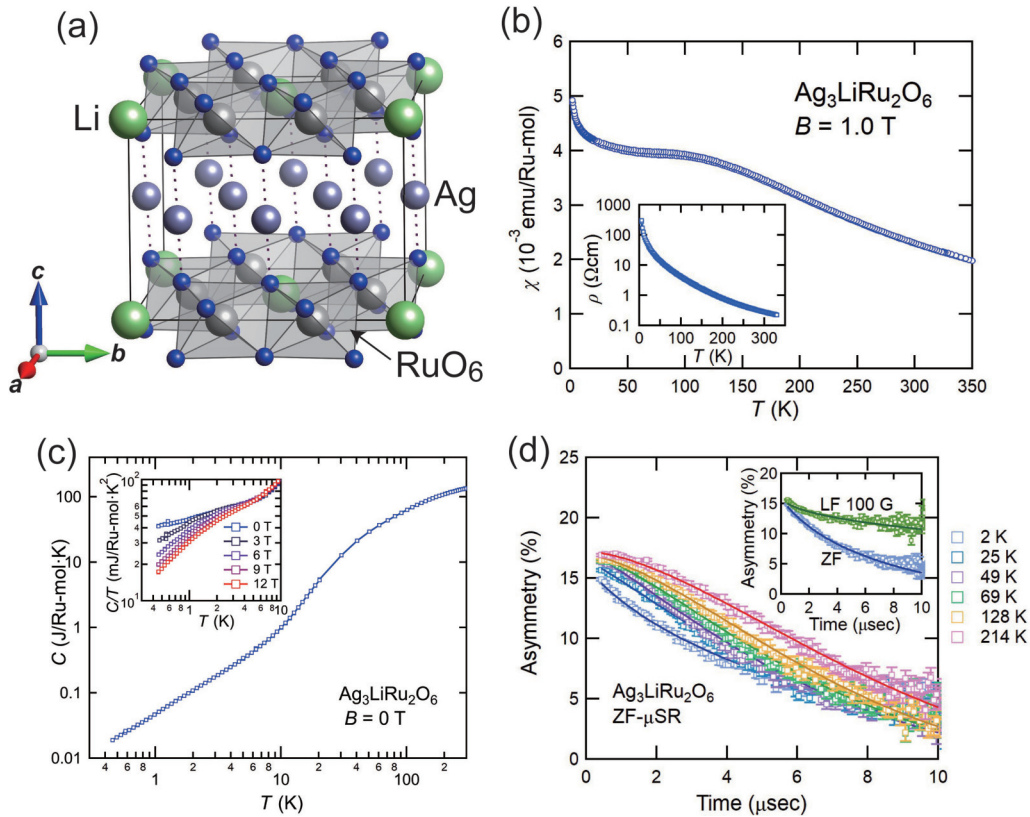


FIG. 1. Absence of magnetic order in the honeycomb ruthenate $\text{Ag}_3\text{LiRu}_2\text{O}_6$. (a) Crystal structure of $\text{Ag}_3\text{LiRu}_2\text{O}_6$. The RuO_6 octahedra compose edge-shared honeycomb layers, and Li ions locate at the center of the honeycomb. Ag ions form O-Ag-O dumbbell bonds between the layers. The crystal structure is visualized by using VESTA software [42]. (b) Magnetic susceptibility $\chi(T)$ of $\text{Ag}_3\text{LiRu}_2\text{O}_6$ powder sample as a function of temperature. The measurement was performed with magnetic field of 1 T. The inset shows the temperature-dependent resistivity. (c) Specific heat $C(T)$ at zero magnetic field. The inset shows the $C(T)/T$ divided by temperature at low temperatures under magnetic fields. The strong suppression of $C(T)/T$ at low temperatures by magnetic fields suggests that the low-temperature contributions originate from localized spin defects. (d) Zero-field (ZF) muon spin relaxation at various temperatures down to 2 K. The inset shows the longitudinal field (LF) measurement with an applied magnetic field of 100 Gauss at 5 K, together with the ZF data at 2 K. The solid lines delineate a fit with a stretched exponential function (see Supplemental Material [43]).

CASSCF and MRCI levels. All computations were performed with the MOLPRO program package [38].

The density functional theory (DFT) band structure calculations were performed for the ambient-pressure and intermediate phases. The crystal structure of the ambient pressure phase is taken from Ref. [19], and the one refined from the neutron diffraction data was used for the intermediate phase. The calculations were performed based on the local density approximation using the fully relativistic linear muffin-tin orbital (LMTO) method implemented in the PY LMTO code [39].

III. RESULTS

A. Crystal structure and electronic structure of $\text{Ag}_3\text{LiRu}_2\text{O}_6$

$\text{Ag}_3\text{LiRu}_2\text{O}_6$ was obtained by an ion-exchange reaction on Li_2RuO_3 . The powder x-ray diffraction indicated that the product is a single phase of $\text{Ag}_3\text{LiRu}_2\text{O}_6$ [19]. The chemical formula of Li_2RuO_3 can be conveniently rewritten as $\frac{1}{2}\text{Li(I)}_3\text{Li(II)Ru}_2\text{O}_6$, where the Li(I) ions occupy the interlayer sites between the Ru-honeycomb layers and Li(II) ion resides at the center of the honeycomb lattice of Ru^{4+} ions.

$\text{Ag}_3\text{LiRu}_2\text{O}_6$ corresponds to the case that all the interlayer Li(I) ions of Li_2RuO_3 are replaced by Ag ions, whereas the $\text{Li(II)Ru}_2^{4+}\text{O}_6$ honeycomb layers remain intact. The full replacement of Li(I) with Ag was confirmed by the structural refinement of powder x-ray diffraction [19]. The structural analysis indicated the presence of strong stacking faults, while the inclusion of Ag ions to the honeycomb layers, which was seen in the similar ion-exchanged compounds [40], was not identified in the transmission electron microscopy investigation [19]. The intercalated Ag^+ ions form covalent O-Ag-O dumbbell bonds with oxygen ions in the $\text{Li(II)Ru}_2\text{O}_6$ layers above and below as in the delafossite oxides [41] [Fig. 1(a)]. Li_2RuO_3 has three inequivalent Ru-Ru bonds on the honeycomb lattice at room temperature, which can be classified into two distinct groups, one short bond with a length of 2.567 Å representing the dimer formation and the other two long bonds with similar lengths of 3.046 and 3.049 Å [15]. In contrast, the Ru honeycomb lattice of $\text{Ag}_3\text{LiRu}_2\text{O}_6$ consists of only two inequivalent Ru-Ru bonds with similar lengths of 3.01(2) and 3.019(10) Å and is thus almost regular [19], indicating the absence of Ru dimerization. We argue that the strong interlayer chemical bond, originating from O 2p and

Ag d_{3z^2-1} orbitals (Fig. S1 in the Supplemental Material [43]), prevents the distortion of the honeycomb lattice and hence suppresses the dimerization.

$\text{Ag}_3\text{LiRu}_2\text{O}_6$ was originally reported to be metallic, based on the reduced resistivity compared with that of Li_2RuO_3 [17]. However, we confirmed the semiconducting behavior of resistivity below room temperature [inset of Fig. 1(b)] with an activation energy $E_a \sim 700$ K at room temperature and the presence of a small charge gap of the order of ~ 0.1 eV in the optical conductivity (Figs. S2 and S3 in the Supplemental Material [43]). The DFT calculation yields a metallic ground state with a relatively high density of states (Fig. S1 in the Supplemental Material [43]). We therefore argue that $\text{Ag}_3\text{LiRu}_2\text{O}_6$ is a weak Mott insulator produced by the moderate electron correlation of Ru $4d$ electrons. The successful analysis of magnetic properties based on the localized $4d^4$ electrons supports further the Mott insulating state of $\text{Ag}_3\text{LiRu}_2\text{O}_6$. The much smaller resistivity compared with that of Li_2RuO_3 may be attributed to the weak Mottness and the absence of large bonding-antibonding splitting of d -electron MOs. The presence of Ag d_{3z^2-1} -O $2p$ antibonding states near the chemical potential may also contribute further to reduce the charge gap.

B. Nonmagnetic ground state at ambient pressure

The absence of strong Ru-Ru dimers in $\text{Ag}_3\text{LiRu}_2\text{O}_6$ appears to restore the magnetism of Ru $4d$ electrons. Figure 1(b) shows magnetic susceptibility $\chi(T)$ of $\text{Ag}_3\text{LiRu}_2\text{O}_6$ powder sample. Here, $\chi(T)$ on cooling from room temperature first shows a Curie-like increase and then crosses over to a temperature-independent paramagnetic susceptibility $< \sim 100$ K as displayed in Fig. 1(b). This behavior is reminiscent of van Vleck susceptibility observed in $J = 0$ Eu^{3+} compounds with $J = 1$ and higher excitations [44], suggesting a spin-orbit-entangled singlet state. No signature of magnetic transition is indeed observed in $\chi(T)$, consistent with the singlet ground state. The small upturn of $\chi(T) < 50$ K is likely attributed to the contributions of spin defects superposed on the van Vleck susceptibility. We speculate that the spin defects mostly originate from the minute amount of Li-Ru disorder inherited from the Li_2RuO_3 precursor (Fig. S4 in the Supplemental Material [43]).

The absence of magnetic order is corroborated indirectly by the specific heat $C(T)$ and directly by the NMR and μSR measurements. The temperature-dependent $C(T)$ shown in Fig. 1(c) does not show any signature of phase transition below room temperature. There is a large T -linear $C(T)$ at low temperatures with a sizable Sommerfeld coefficient $\gamma \sim 40$ mJ Ru-mol $^{-1}$ K $^{-2}$ at zero field. This contribution is readily suppressed by applying a magnetic field roughly up to a temperature corresponding to the Zeeman energy [the inset of Fig. 1(c)]. Considering the nonmagnetic insulating state with a sizable magnetic excitation gap (see below), the magnetic field suppression scaled by the Zeeman energy implies that it originates predominantly from spin defects as found in the low-temperature $\chi(T)$.

The ^7Li -NMR spectrum on the powder sample at room temperature shows a quite asymmetric lineshape, which we ascribe to anisotropy of Knight shift (Figs. 3(b) and S5 and S6 in the Supplemental Material [43]). There is only one Li crys-

tallographic site in $\text{Ag}_3\text{LiRu}_2\text{O}_6$, and intersite mixing between Li and Ag was not identified in the analysis of powder x-ray diffraction [19]. Upon cooling, the asymmetry increases, but no splitting is observed down to 5 K, demonstrating the absence of magnetic ordering. In the corresponding spin-lattice relaxation rate $1/T_1$ shown in Fig. 2(c), no divergence indicative of magnetic phase transition is observed. The broad peak at a low temperature can be ascribed to contributions from magnetic defects seen in $\chi(T)$ and $C(T)$.

The time dependence of muon asymmetry [Fig. 1(d)] shows a monotonic decrease without any oscillatory signals, again reinforcing the absence of magnetic order. The time spectra show the Gaussian shape at high temperatures, whereas they change into an exponential curve < 25 K (Table S1 and Fig. S7 in the Supplemental Material [43]). This behavior is reminiscent of slowing down of spin fluctuations. However, the relaxation at low temperatures is suppressed by the application of a small LF of 100 Gauss, as shown in the inset of Fig. 1(d). This indicates that the internal field at the muon sites is quite small and of the order of nuclear dipole fields. The slow relaxation under LF shows a stretched exponent behavior $\exp\{-(\lambda t)^\beta\}$ with $\beta \sim 0.5$. This suggests that the dynamical relaxation is not homogeneous, likely associated with dilute defect spins in a nonmagnetic state. This is in line with the spin defect picture which has emerged from the other probes.

C. Spin-orbit-entangled singlet state at ambient pressure

The nonmagnetic state with van Vleck-like behavior of $\chi(T)$ strongly suggests a spin-orbit-entangled singlet ground state in $\text{Ag}_3\text{LiRu}_2\text{O}_6$, which is characterized by the presence of a small excitation gap to $J_{\text{eff}} = 1$ states of the order of SOC. The presence of a magnetic excitation gap of 35 meV is indeed identified by time-of-flight powder INS. Figure 2(a) shows the two-dimensional map of scattering intensities after subtracting the phonon contribution. There is an intense signal centered at ~ 35 meV in the region of small momentum transfer $|Q|$, and its intensity decreases quickly as $|Q|$ increases, indicating the magnetic origin of excitation. This excitation appears as a broad peak in the imaginary part of dynamic susceptibility $\chi''(\mathbf{Q}, E) \propto \{1 - \exp(-E/k_B T)\} S(\mathbf{Q}, E)$ [Fig. 2(b), where $S(\mathbf{Q}, E)$ is the dynamic correlation function] integrated in the small $|Q|$ region (1.5 – 1.9 \AA^{-1}). The intensity monotonically decreases on heating, but the peak is visible even at 200 K.

The presence of a magnetic excitation gap is also confirmed in the temperature dependence of spin lattice relaxation rate $1/T_1$ from ^7Li -NMR. As seen in Fig. 2(c), $1/T_1$ exhibits a complex temperature dependence: on cooling from room temperature, $1/T_1$ decreases rapidly and then shows a dip at ~ 50 K followed by a broad peak at ~ 10 K, which we attributed to the low-lying excitations associated with the defect spins, mostly due to the Li-Ru disorder. The rapid decrease of $1/T_1$ below room temperature is incompatible with a Curie-Weiss behavior of localized moments, supporting that the increase of $\chi(T)$ around room temperature originates from the van Vleck susceptibility and therefore should be ascribed to the magnetic excitation predominantly to $J_{\text{eff}} = 1$ states.

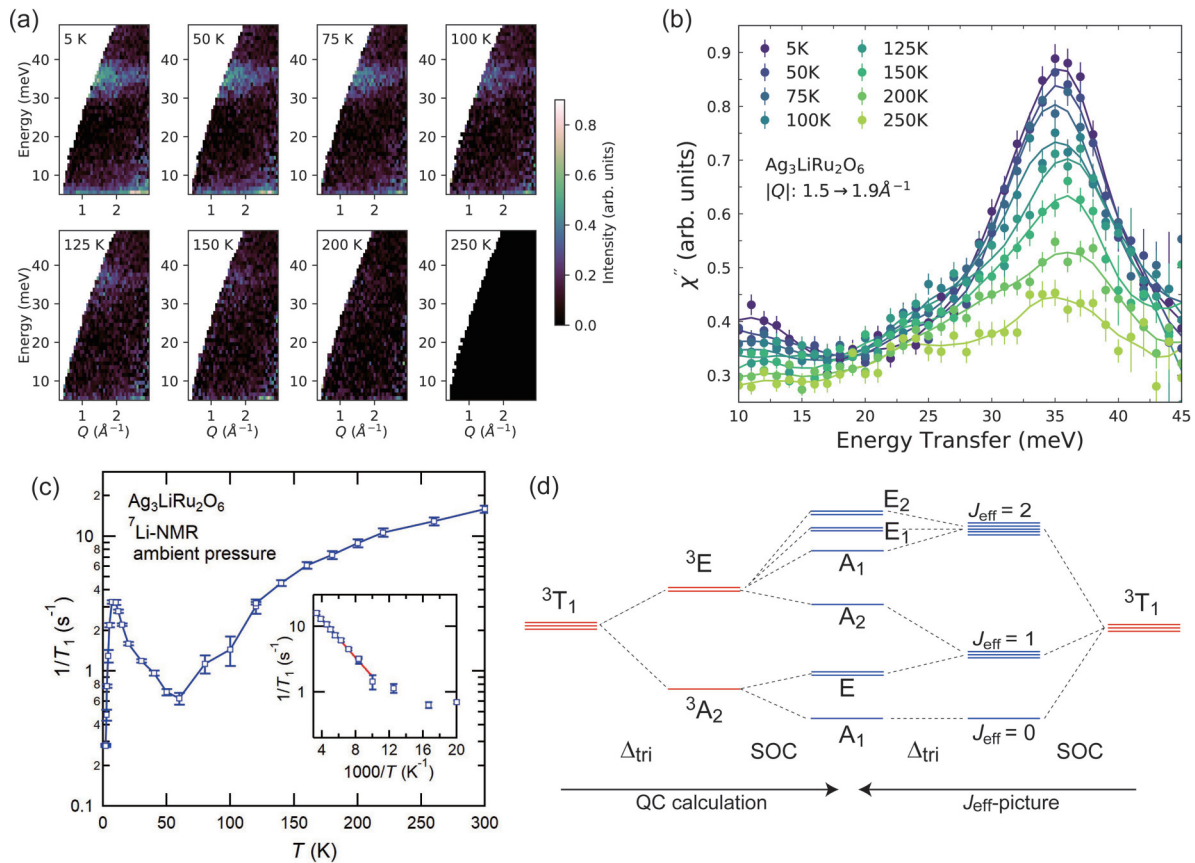


FIG. 2. Spin-orbit-entangled singlet state in $\text{Ag}_3\text{LiRu}_2\text{O}_6$ at ambient pressure. (a) Inelastic neutron scattering (INS) on the powder sample of $\text{Ag}_3\text{LiRu}_2\text{O}_6$. The figures show the contour plot of scattering intensities where the phonon contribution was removed by subtracting the temperature-scaled 250 K dataset. The raw data are shown in Fig. S8 in the Supplemental Material [43]. (b) The imaginary part of the dynamic susceptibility χ'' as a function of energy transfer in the $|Q|$ region between 1.5 and 1.9 \AA^{-1} at various temperatures. (c) Inverse of ^7Li -NMR spin-lattice relaxation time T_1 as a function of temperature. T_1 is measured at the larger shift peak of spectra [see Fig. 3(b)]. The inset shows the Arrhenius plot of the data, and the red line represents the fit between 100 and 300 K. The fit gives a gap of ~ 30 meV. The peak of $1/T_1$ at ~ 10 K is likely attributed to the localized spin defects observed in $\chi(T)$ and $C(T)$. (d) Schematic energy levels of $\text{Ru}^{4+} t_{2g}^4$ states obtained by the quantum chemistry (QC) calculation (from left to middle). The states expressed by the red bar are threefold degenerate because of $S = 1$, while those of the blue bar represent a single state. Each state is labeled with a Mulliken symbol. The nine states of 3T_1 split by trigonal crystal field (Δ_{tri}) into the 3A_2 and 3E states. Spin-orbit coupling (SOC) further splits those states and yields the A_1 singlet ground state. The diagram from right to middle shows the J_{eff} picture where SOC first splits the 3T_1 states into $J_{\text{eff}} = 0, 1$, and 2 states and Δ_{tri} acts on the J_{eff} states. The resultant energy diagram is identical in both representations.

The Arrhenius plot of $1/T_1 > 100$ K, shown in the inset of Fig. 2(c), yields a gap of ~ 30 meV, close to the one observed in INS. The gap between the $J_{\text{eff}} = 0$ singlet and the $J_{\text{eff}} = 1$ triplet corresponds to λ_{SO} ($\lambda_{\text{SO}} = \zeta/2S$, where ζ is the single-electron SOC and $S = 1$). The free-electron value of ζ for Ru is ~ 140 meV, and thus, the expected gap is ~ 70 meV, as observed in a $J_{\text{eff}} = 0$ Mott insulator K_2RuCl_6 [45]. This gap value is much larger than ~ 35 meV observed in $\text{Ag}_3\text{LiRu}_2\text{O}_6$. We argue that the trigonal distortion of the RuO_6 octahedra splits the $J_{\text{eff}} = 1$ triplet into a singlet and doublet and reduces the lowest excitation gap, as schematically illustrated in Fig. 2(d). Essentially the same mechanism of gap reduction was discussed in Ca_2RuO_4 hosting tetragonally distorted RuO_6 octahedra [9].

Embedded cluster quantum chemistry calculations of electronic structure were performed with the CASSCF and MRCI methods and give the energy level scheme summarized in

Fig. 2(d) (from left to middle) and Table I. The calculations without SOC show that the t_{2g}^4 multiplet of a Ru^{4+} ion with $S = 1$ and $L_{\text{eff}} = 1$ (3T_1) splits into the lower 3A_2 and upper 3E states in the presence of a trigonal crystal field. The two methods yield very close results, and we hereafter refer only to the one obtained by the more accurate MRCI treatment. The splitting of 3A_2 and 3E is ~ 120 meV, which is reasonable in magnitude as the trigonal crystal field splitting of t_{2g} multiplet in $4d$ transition-metal oxides with an octahedral coordination. There is an additional small split of the originally degenerate 3E state due to the presence of a nontrigonal crystal field originating from the monoclinic distortion, which we ignore in the following discussion for simplicity. This small split can be found in Table I and is indeed negligibly small as compared with the trigonal field splitting. By incorporating SOC, the 3A_2 state splits into the ground state A_1 singlet and the upper E doublet ~ 47 meV above A_1 . The higher 3E doublet by

TABLE I. Energy levels of $\text{Ru}^{4+} t_{2g}^4$ states by crystal field and SOC in $\text{Ag}_3\text{LiRu}_2\text{O}_6$. The energy of multiplets is obtained from the embedded cluster CASSCF(4e, 5o), denoted as CAS in the table, and MRCI calculations, with and without incorporating SOC. The energy of the lowest state is set to be zero, and the energy gaps from the lowest state are shown. The calculation was performed for the crystal structure at room temperature reported in Ref. [17]. The nine states of t_{2g}^4 configuration (3T_1 with $S = 1, L = 1$) are split into 3A_2 (3 states) and 3E (6 states) by trigonal crystal field. SOC further splits the 3A_2 (3E) states into A_1 singlet and E doublets (A_2 and A_1 singlets, E_1 and E_2 doublets), respectively [see Fig. 2(d) as well]. This gives rise to a gap of ~ 47 meV between the ground state singlet A_1 and the lowest doublet E . Note that there is a small split within the E doublets because of weak nontrigonal distortion.

CAS (meV)	CAS + SOC (meV)	MRCI (meV)	MRCI + SOC (meV)
${}^3A_2: 0$	$A_1: 0$ $E: 49.7, 51.3$	${}^3A_2: 0$	$A_1: 0$ $E: 46.5, 48.1$
${}^3E: 107.1, 115.5$	$A_2: 139.1$ $A_1: 198.5$ $E_1: 212.0, 218.8$ $E_2: 235.1, 235.2$	${}^3E: 119.7, 129.6$	$A_2: 147.6$ $A_1: 200.1$ $E_1: 216.0, 224.3$ $E_2: 241.5, 241.6$

SOC into the two singlets (A_2 and A_1 at ~ 148 and ~ 200 meV above the ground state A_1 singlet, respectively) and two doublets (E_1 and E_2 at ~ 220 and ~ 240 meV, respectively). The singlet A_2 is the lowest excited state out of the 3E state. In the J_{eff} language [depicted in Fig. 2(d) from right to middle], the ground state A_1 singlet originates from the $J_{\text{eff}} = 0$ state, and the low-lying excited states, the E doublet and A_2 singlet, originate from the $J_{\text{eff}} = 1$ triplet. That is, the $J_{\text{eff}} = 1$ triplet splits into the lower E doublet at ~ 47 meV and the upper A_2 singlet at ~ 148 meV with the trigonal crystal field. We note that the A_1 singlet ground state is no longer a pure $J_{\text{eff}} = 0$ state in the presence of trigonal distortion.

The calculated A_1 singlet– E doublet gap of ~ 47 meV agrees reasonably with the excitation gap ~ 35 meV seen in the INS measurement. We do not resolve clear dispersion in the ~ 35 meV excitation in the INS data with ~ 10 meV width, which may suggest a small exchange coupling and negligible dispersion of excited states as compared with the excitation gap. From these experimental and theoretical results, we conclude that the ambient pressure phase of $\text{Ag}_3\text{LiRu}_2\text{O}_6$ is a $J_{\text{eff}} = 0$ -derived spin-orbit-entangled singlet state, which we call the J -singlet state hereafter.

D. Pressure-induced phase transitions

To explore the possible excitonic magnetism and other exotic states out of the J -singlet state, we attempted to enhance the exchange interactions by applying pressure. At ambient pressure, $\chi(T)$ shows van Vleck-like behavior as discussed above. With the application of pressure, $\chi(T)$ shows a drastic change, as shown in Fig. 3(a). At 0.38 GPa, $\chi(T)$ displays a shoulderlike anomaly at ~ 150 K and shows an almost temperature-independent behavior at lower temperatures, indicative of a pressure-induced transition. The transition temperature, defined as the temperature for the $\chi(T)$ anomaly, increases rapidly to almost room temperature with increasing pressure > 1 GPa. The temperature-dependent resistivity does not change appreciably under pressure with no clear anomaly at the transition (Fig. S9 in the Supplemental Material [43]).

The pressure-induced phase, which we call an intermediate phase because of the presence of another phase at a higher pressure, is nonmagnetic and not an excitonic magnet with

closed gap. ${}^7\text{Li}$ -NMR spectra under pressure in Fig. 3(b) indicate the absence of magnetic order in the intermediate phase. At $P = 0.9$ GPa, the asymmetric spectrum around room temperature does not change substantially from that at ambient pressure. However, below 200 K where the $\chi(T)$ anomaly is seen at a similar pressure [0.83 GPa in Fig. 3(a)], the asymmetric peak fades out and is replaced by one symmetric peak with a small shift at low temperatures, supportive of the occurrence of phase transition at ~ 200 K. The spectrum at ~ 200 K comprises the superposition of the high-temperature asymmetric peak and the low-temperature symmetric peak, which indicates the two-phase coexistence and hence the first-order nature of the transition. The symmetric peak in the intermediate phase remains relatively sharp down to the lowest temperature, excluding a magnetic order. The absence of magnetic order is also corroborated by the ZF- μSR measurement performed in the intermediate phase down to 2 K at 0.64 GPa, where no signature of coherent muon-spin precession was found (Fig. S10 in the Supplemental Material [43]). At 3.1 GPa, the NMR spectra for the intermediate phase persists up to room temperature, meaning that the phase transition temperature, if any, is above room temperature.

Interestingly, the excitation gap estimated from $1/T_1$ in the intermediate phase is not appreciably different from that of the J -singlet phase at ambient pressure. Figure 3(c) shows the temperature dependence of $1/T_1$ under pressure. The gap size remains ~ 30 meV, as estimated from the Arrhenius plot at 0.9 GPa between 200 and 100 K and at 3.1 GPa [the inset of Fig. 3(c)]. This suggests that the nature of the intermediate phase should be closely related to that of the J -singlet phase. A broad peak of $1/T_1$ at low temperatures remains to be seen under pressure. This suggests that the spin defects, likely originating from the Li-Ru disorder, are retained regardless of the nature of nonmagnetic background.

By further increasing pressure to 4.5 GPa, the ${}^7\text{Li}$ -NMR spectrum shows a substantial change, indicative of another pressure-induced phase transition. The peak becomes much sharper compared with those at lower pressures, and the peak position, i.e., the Knight shift, is close to zero and independent of temperature. Such a sharp and zero-shift peak has been observed in the dimerized state of Li_2RuO_3 [46], owing to the almost complete absence of internal magnetic fields

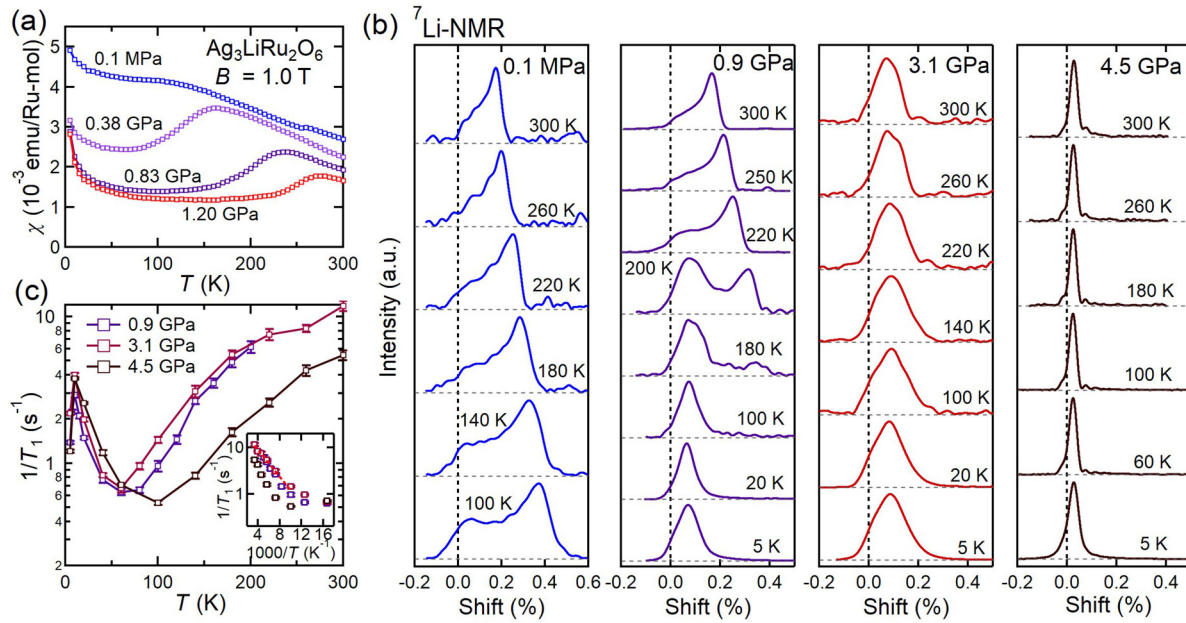


FIG. 3. Pressure-induced change of magnetism in $\text{Ag}_3\text{LiRu}_2\text{O}_6$. (a) Magnetic susceptibility $\chi(T)$ under pressure. The measurements were performed at magnetic field of 1 T. (b) ^7Li -nuclear magnetic resonance (NMR) spectra at various pressures. The two-peak structure at ambient pressure likely originates from the strong magnetic anisotropy (see Figs. S5 and S6 in the Supplemental Material [43]). At 0.9 GPa, a change of spectrum from an asymmetric shape to a symmetric and lower shift peak was seen on cooling <200 K. The spectra at 0.9 and 3.1 GPa at low temperatures remain sharp, pointing to a nonmagnetic nature of the intermediate phase. At 4.5 GPa, the spectra become much sharper than the lower pressure data. (c) Inverse of spin-lattice relaxation time T_1 under pressure obtained from ^7Li -NMR. The $1/T_1$ at 0.9 GPa was obtained at the smaller shift peak <200 K. The inset shows the Arrhenius plot of $1/T_1$ where the similar gapped behavior as in the ambient pressure phase is seen. The dotted line shows a fit for the 3.1 GPa data between 300 and 100 K. The estimated gap sizes at 0.9 and 3.1 GPa are nearly the same (~ 30 meV), while the one at 4.5 GPa is larger (~ 48 meV), implying a different origin of excitation gap.

from electron spins. This suggests the formation of strong dimers up to room temperature at 4.5 GPa. In accord with this, $1/T_1 > 100$ K is strongly suppressed compared with those of the ambient pressure and the intermediate phases and shows the enhanced excitation gap of ~ 48 meV. This indicates that another pressure-induced phase with a distinct excitation gap, which we call high-pressure phase, is realized at ~ 4.5 GPa.

Neutron diffraction under pressure reveals that the two pressure-induced phase transitions, identified in $\chi(T)$ and NMR, are accompanied by a structural change. The lattice parameters at room temperature under pressure were refined using the monoclinic unit cell of the ambient pressure phase, which is displayed in Fig. 4(a) as a function of pressure. The a and b axes are in the honeycomb plane, along one of the Ru zigzag chains of the honeycomb lattice and parallel to the bridging Ru-Ru bonds, respectively, as depicted in Fig. 4(b). The c axis defines the out-of-plane direction. The in-plane lattice constants a and b decrease with pressure, while c and the monoclinic angle β remain almost constant up to ~ 4 GPa. At ~ 1.8 GPa, a shows a discontinuous drop, indicating the presence of a first-order structural transition. By increasing pressure further, another sudden change of lattice parameters is observed at ~ 4.5 GPa, where a shrinks further and c and β increase. Upon cooling, the critical pressures for the two structural transitions are reduced (Fig. S11 in the Supplemental Material [43]). The critical pressures for the first structural transition agree reasonably with those determined from $\chi(T)$,

as depicted in the phase diagram shown in Fig. 5, indicating that the transition to the intermediate phase is accompanied by the first structural transition. The second transition represents the sharpening of ^7Li -NMR spectra observed at 4.5 GPa, namely, the transition from the intermediate phase to the high-pressure phase.

The crystal structure of the intermediate phase was refined reasonably by the same structural model with that at ambient pressure (Table S2 in the Supplemental Material [43]). While there is no pronounced change in the distortion of RuO_6 octahedra (Fig. S12 in the Supplemental Material [43]), the honeycomb lattice of Ru atoms is weakly squashed along the a axis. The Ru honeycomb lattice refined at 200 K and 3.1 GPa is illustrated in Fig. 4(b), together with that at ambient pressure [19]. The angle of Ru-Ru bonds along the zigzag chains is decreased to $\sim 116^\circ$ from $\sim 120^\circ$ at ambient pressure, which results in the shortening of the bridging Ru-Ru bonds along the b axis by $\sim 4\%$ compared with the other bonds in the zigzag chain. Hence, this intermediate phase is characterized by the presence of weak Ru-Ru dimers along the b axis.

The drastic sharpening of NMR linewidth at 4.5 GPa suggests the change of the electronic ground state through the second structural transition. The refinement of the neutron diffraction pattern in the high-pressure phase was not successful with using the structural model of the intermediate phase, implying a distinct distortion of the Ru honeycomb lattice. To investigate the distortion, XAFS spectra at the Ru K -edge were collected under pressure. Figure 4(c) shows

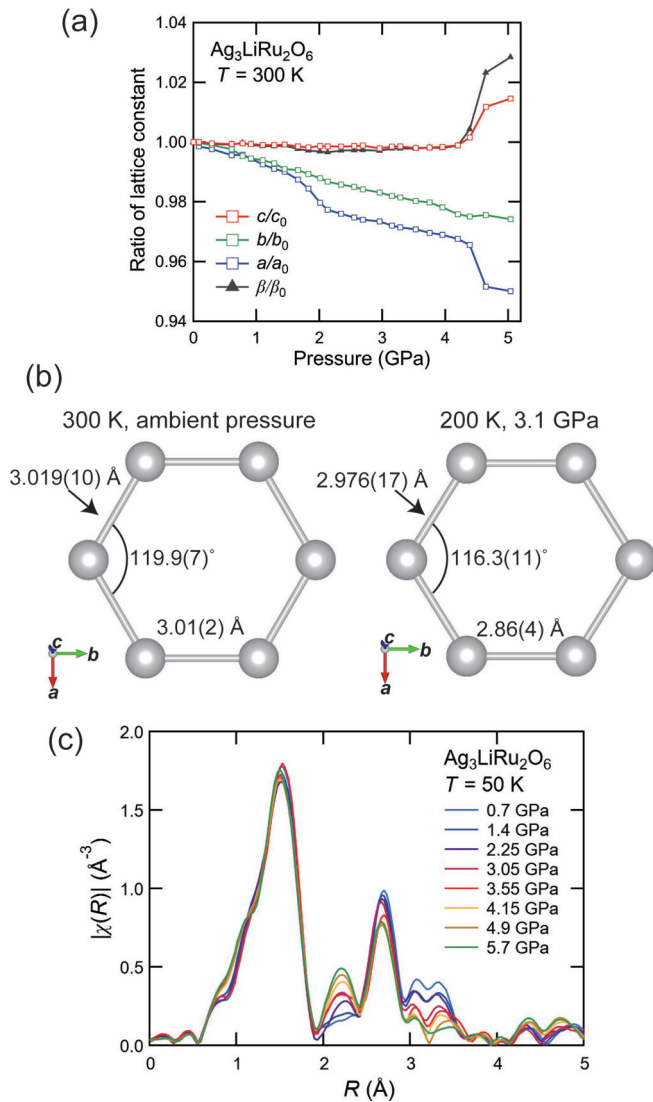


FIG. 4. Pressure-induced structural transitions in $\text{Ag}_3\text{LiRu}_2\text{O}_6$. (a) Pressure-dependent lattice parameters at room temperature obtained from neutron diffraction. The values of lattice constants are evaluated using the monoclinic unit cell of the ambient pressure phase (space group $C2/m$) and normalized by those at ambient pressure. (b) Ru honeycomb lattices at ambient pressure (left) and in the intermediate phase (right). The structure at ambient pressure is taken from Ref. [19], and the one in the intermediate phase was obtained from the Rietveld refinement of neutron diffraction at 200 K and at 3.1 GPa. (c) The magnitude of the complex Fourier transform (FT) of x-ray absorption fine structure (XAFS) data for various pressures at $T = 50$ K. Note that the FT is not corrected for scattering phase shifts, and the R values do not exactly correspond to the bond lengths.

the Fourier transform (FT) magnitude of the complex XAFS function at 50 K, related to the partial radial distribution function of Ru atoms. The peak at $R \sim 1.5$ Å represents the Ru-O bonds, while that at ~ 2.7 Å corresponds to the Ru-Ru distance. Note that FT data shown in Fig. 4(c) are not corrected for photoelectron scattering phase shifts in the central and neighboring atoms, and thus, the peaks in the FT are shifted to smaller distances. By inspecting the peak intensities at ~ 2.7 Å, a clear difference is seen between the

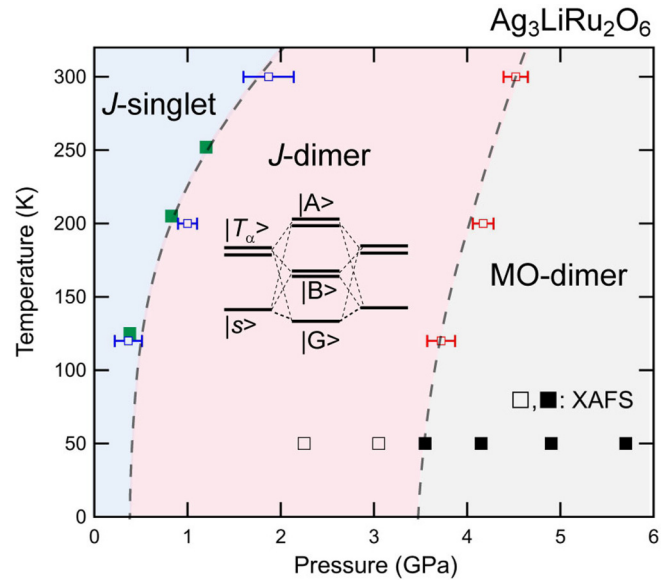


FIG. 5. Pressure-temperature phase diagram of $\text{Ag}_3\text{LiRu}_2\text{O}_6$. The blue and red open squares represent the phase boundaries determined by the neutron diffraction, whereas the green squares show the transition temperatures determined by $d\chi(T)/dT$. The filled (open) black squares indicate the points where the strong dimerization of Ru atoms was found in the x-ray absorption fine structure (XAFS) spectra in the high-pressure (intermediate) phases, respectively. The inset depicts the J -dimer model of the intermediate phase. On each site, we consider a singlet $|s\rangle$ and upper doublet $|T_\alpha\rangle$ ($\alpha = x, y$) which is split from the $J_{\text{eff}} = 1$ triplet by trigonal crystal field. These states form the ground state $|G\rangle$, bonding states $|B\rangle$, and antibonding states $|A\rangle$ by exchange interactions. In the full J -dimer model including the upper singlet $|T_z\rangle$, there are 16 states per dimer in total, but we show here only the lower five states for brevity. See Supplemental Material [43] for more discussions about the J -dimer model.

pressure values < 3.05 GPa and > 4.15 GPa. The structural transition appears to occur at ~ 3.5 GPa, which agrees with the phase boundary estimated from the neutron diffraction results (Fig. 5). In the high-pressure phase, the growth of the peak is seen at $R \sim 2.2$ Å. This peak may indicate the shortening of the Ru-Ru distance. We analyzed the data at 5.7 GPa with the strong dimer model like the structure of Li_2RuO_3 , where a Ru hexagon is composed of two short bonds and four long bonds. The refinement of FT data gives the Ru-Ru distances of 2.51(2) and 3.06(2) Å for the short and long bonds, respectively (Fig. S13 in the Supplemental Material [43]). The difference of bond lengths is $\sim 19\%$, which is close to that in Li_2RuO_3 ($\sim 17\%$), indicating the formation of strong Ru-Ru dimers induced by pressure. We note that the peak at ~ 2.2 Å starts to grow already at ~ 2.3 GPa, i.e., in the intermediate phase. This may indicate that local dimerization takes place partially in the intermediate phase or that fluctuating dimers are present as a precursor of strong dimers, as discussed in the high-temperature phase of Li_2RuO_3 [47].

IV. DISCUSSION

The honeycomb ruthenate $\text{Ag}_3\text{LiRu}_2\text{O}_6$ was found to host a spin-orbit-entangled J -singlet state, proximate to the $J_{\text{eff}} =$

0 state, at ambient pressure. This state is realized by suppressing the Ru-Ru dimerization that takes place in Li_2RuO_3 . The honeycomb lattice of the spin-orbit-entangled singlet is expected to display frustrated excitonic magnetism such as a spin-nematic state and the bosonic Kitaev liquid. However, the J -singlet state remains intact down to the lowest temperature measured at ambient pressure without any discernible changes in the magnetic excitation spectra. This is likely because the exchange interactions via the upper doublet, derived from the $J_{\text{eff}} = 1$ triplet, are not strong enough. To realize the excitonic magnetism, enhancement of exchange interactions and/or the reduction of the singlet-doublet gap with a stronger trigonal crystal field would be required.

Upon the application of pressure, the Ru honeycomb lattice of $\text{Ag}_3\text{LiRu}_2\text{O}_6$ first shrinks almost isotropically [Fig. 4(a)]. In tandem with this, magnetic susceptibility at room temperature decreases monotonically up to ~ 1.2 GPa [Fig. 3(a)], implying an enhancement of antiferromagnetic interactions. By further increasing pressure, instead of developing excitonic magnetism, $\text{Ag}_3\text{LiRu}_2\text{O}_6$ exhibits successive phase transitions to other nonmagnetic phases. The first transition to the intermediate phase at ~ 1.8 GPa at room temperature is characterized by the modest squashing of the Ru honeycomb lattice along the a axis and the formation of weak Ru-Ru dimers along the b axis. The intermediate phase was found to be nonmagnetic by the ^7Li -NMR and μSR measurements.

The second transition to the high-pressure phase appears at ~ 4.5 GPa at room temperature, accompanied by the formation of strong Ru-Ru dimers with very short bond lengths. This dimer phase is reminiscent of the low-temperature phase of Li_2RuO_3 where the large bonding-antibonding split of d -electron MOs stabilizes the strong Ru-Ru dimers [15,16]. The spin and orbital degrees of freedom are fully quenched in the MOs, leading to a nonmagnetic ground state. The sharp and almost zero shift ^7Li -NMR peak observed at 4.5 GPa indicates that such a MO state is also present in the high-pressure phase of $\text{Ag}_3\text{LiRu}_2\text{O}_6$. We call the high-pressure phase of $\text{Ag}_3\text{LiRu}_2\text{O}_6$ the MO-dimer state. A pressure-induced strong dimerization like $\text{Ag}_3\text{LiRu}_2\text{O}_6$ was also observed in the honeycomb iridates $\alpha, \beta\text{-Li}_2\text{IrO}_3$ [48,49], and $\alpha\text{-RuCl}_3$ [50], indicating that the competition between spin-orbital entanglement and a MO state is common in SOC honeycomb compounds.

The nature of the intermediate phase is distinct from the high-pressure phase with the MO dimers. The magnetic susceptibility $\chi(T)$ of the intermediate phase is $\sim 1.5 \times 10^{-3}$ emu/Ru-mol from the data at 1.20 GPa, which is much larger than that of the MO phase of Li_2RuO_3 ($\sim 0.3 \times 10^{-3}$ emu/Ru-mol [15]). While the intermediate phase is nonmagnetic, the ^7Li -NMR spectra are broader than those in the high-pressure phase, which may indicate nonnegligible magnetic anisotropy and that the SOC is not quenched. The DFT calculations on this phase point to a metallic state despite the insulating behavior of the resistivity, suggesting a Mott insulating state (Fig. S15 in the Supplemental Material [43]). This contrasts with the systems with strong dimers where DFT calculations yield a band-insulating ground state associated with MO formation [16,49,51]. These facts suggest that the weak dimers of the intermediate phase do not involve the formation of MOs. The excitation gap of the intermediate phase,

which is close to that of the ambient pressure phase estimated from the NMR $1/T_1$ [Fig. 3(c)], implies that the intermediate phase maintains a character of a spin-orbit-entangled singlet state where the excitation gap is mostly determined by the strength of SOC, but the weak-dimer distortion lowers further the energy of the singlet ground state.

The basic electronic structure of the intermediate phase, associated with the weak dimer of the J -singlet states, can be understood as schematically illustrated in the inset of Fig. 5. The short Ru-Ru distance should enhance the exchange interactions on the weak dimer bonds, which leads to the split of excited triplet states into the states with bonding and antibonding characters (Fig. S16 in the Supplemental Material [43]) and more importantly allows the hybridization between the ground state singlet and the excited triplet states. The ground state $|G\rangle$ consists of a pair of singlets $|ss\rangle$ with a small admixture of triplet pairs $|T_\alpha T_\alpha\rangle$, where T_α denotes the triplet with three different components $\alpha = x, y, \text{ and } z$ [7,12]. The bonding $|B\rangle$ (antibonding $|A\rangle$) states comprise the singlet and triplet pairs, $|sT_\alpha\rangle - |T_\alpha s\rangle$ ($|sT_\alpha\rangle + |T_\alpha s\rangle$), respectively (Table S3 in the Supplemental Material [43]). In $\text{Ag}_3\text{LiRu}_2\text{O}_6$, the $J_{\text{eff}} = 1$ triplet splits into the lower doublet and the upper singlet by the trigonal crystal field. Nevertheless, the lower doublet similarly forms the bonding and antibonding states, as depicted in the inset of Fig. 5 and Fig. S17 in the Supplemental Material [43]. We call this picture of the intermediate phase the J -dimer state. While both the J -singlet and J -dimer states are spin-orbital singlets, the lattice distortion of the J -dimer state renders the admixture of low-lying excited states derived from the $J_{\text{eff}} = 1$ triplet into the ground state singlet and lowers its energy, which can be viewed as a pseudo-JT effect [52]. Such weak-dimer distortion has not been observed in d^5 honeycomb-based iridates and $\alpha\text{-RuCl}_3$ under pressure, particularly in $\text{Ag}_3\text{LiIr}_2\text{O}_6$ (Fig. S14 in the Supplemental Material [43]) and Cu_2IrO_3 [53], comprising interlayer dumbbell bonds like those of $\text{Ag}_3\text{LiRu}_2\text{O}_6$. From this, we infer that the weak-dimer distortion is induced by the pseudo-JT effect with the presence of low-lying spin-orbital-excited states rather than structural instability and thus is unique to d^4 honeycomb systems.

The apparent decrease of low-temperature $\chi(T)$ from the ambient-pressure J -singlet state to the intermediate phase, if it is dominated by the van Vleck process, indicates the increase of the excitation gap, in contrast to the robust gap magnitude estimated from $1/T_1$. The J -dimer model described above can reasonably explain the contrasted behavior of $\chi(T)$ and $1/T_1$. In the J -dimer state, there are two low-energy magnetic excitations, from $|G\rangle$ to $|B\rangle$ and to $|A\rangle$. Under a magnetic field, there is a finite mixing between $|G\rangle$ and $|A\rangle$ but not between $|G\rangle$ and $|B\rangle$ (Table S4 in the Supplemental Material [43]). The mixing between $|G\rangle$ and $|A\rangle$, with a larger gap than that between $|G\rangle$ and $|B\rangle$, therefore determines the van Vleck magnetic susceptibility. On the other hand, NMR $1/T_1$, which is in proportion to the q -integrated imaginary part of dynamical susceptibility, should capture both $|B\rangle$ and $|A\rangle$ excitations. The magnitude of excitation gap estimated from $1/T_1$ in the intermediate phase should reflect the average of the excitations to $|B\rangle$ and to $|A\rangle$ and thus not be so different from that at ambient pressure. In fact, the energy level splitting of the J -dimer model depends on the dominant exchange interac-

tions: the Kitaev-type exchange acts on only one component of the triplet ($|T_z\rangle$ along the z bond), while all components are involved in the Heisenberg-type coupling (Fig. S16 in the Supplemental Material [43]). The measurement of a detailed excitation spectrum in the intermediate phase should provide further support for the proposed J -dimer state and information about the dominant exchange interaction.

V. CONCLUSIONS

A honeycomb lattice of spin-orbit-entangled singlets was identified in $\text{Ag}_3\text{LiRu}_2\text{O}_6$ with $4d^4$ Ru^{4+} ions, indicating that honeycomb ruthenates are a promising candidate system to realize unconventional excitonic magnetic phases. $\text{Ag}_3\text{LiRu}_2\text{O}_6$ is a nonmagnetic Mott insulator with a $J_{\text{eff}} = 0$ -derived J -singlet state at ambient pressure due to small exchange interactions through the excited $J_{\text{eff}} = 1$ -derived states. By application of pressure, $\text{Ag}_3\text{LiRu}_2\text{O}_6$ displays successive phase transitions to other nonmagnetic phases instead of developing excitonic magnetism. While the high-pressure MO phase is analogous to those identified in other honeycomb-based materials, the intermediate phase with weak dimers is unique to this honeycomb ruthenate. We propose that the intermediate phase represents the SOC J -dimer state which has not been predicted in theory. We speculate that the J -dimer state is induced by a pseudo-JT effect associated with low-lying spin-orbital excitations. The pseudo-JT effect, which is potentially

inherent in spin-orbit-entangled d^4 compounds, may compete with the development of frustrated excitonic magnetism. Therefore, the role of the lattice degree of freedom should be explicitly considered for further materials design. We believe this finding will open up a pathway for rich physics of $J_{\text{eff}} = 0$ -based honeycomb systems as have been established in the celebrated $J_{\text{eff}} = \frac{1}{2}$ Kitaev materials [4,5].

ACKNOWLEDGMENTS

We are grateful to G. Khaliullin, J. Chaloupka, G. Jackeli, and M. D. Le for invaluable discussions. We acknowledge the provision of beamtimes on PEARL (Proposal No. RB1920241 [54]) and MAPS (Proposal No. RB1820520 [55]) to Science & Technology Facilities Council (STFC). We thank the RIKEN-RAL muon facilities for the allocation of beamtime on ARGUS at ISIS Neutron and Muon Source (Proposal No. RB1970001 [56]). We thank the National Synchrotron Radiation Research Center and the Japan Synchrotron Radiation Research Institute for the allocation of beamtime for high-pressure x-ray diffraction measurements at BL12B2 of SPring-8 (Proposal No. 2018B4139). Work at Argonne is supported by the U.S. Department of Energy, Office of Science, Office of Basic Energy Sciences, under Contract No. DE-AC-02-06CH11357. We thank PRIUS for providing NPD anvils. W.B. acknowledges partial support by the Consortium for Materials Properties Research in Earth Sciences. This paper is partly supported by the Alexander von Humboldt Foundation.

-
- [1] A. Abragam and B. Bleaney, *Electron Paramagnetic Resonance of Transition Ions* (Clarendon Press, Oxford, 1970).
- [2] T. Takayama, J. Chaloupka, A. Smerald, G. Khaliullin, and H. Takagi, Spin-orbit-entangled electronic phases in $4d$ and $5d$ transition-metal compounds, *J. Phys. Soc. Jpn.* **90**, 062001 (2021).
- [3] G. Khaliullin, Orbital order and fluctuations in Mott insulators, *Prog. Theor. Phys. Suppl.* **160**, 155 (2005).
- [4] G. Jackeli and G. Khaliullin, Mott Insulators in the Strong Spin-Orbit Coupling Limit: From Heisenberg to a Quantum Compass and Kitaev Models, *Phys. Rev. Lett.* **102**, 017205 (2009).
- [5] H. Takagi, T. Takayama, G. Jackeli, G. Khaliullin, and S. E. Nagler, Concept and realization of Kitaev quantum spin liquids, *Nat. Rev. Phys.* **1**, 264 (2019).
- [6] M. G. Yamada, M. Oshikawa, and G. Jackeli, Emergent $SU(4)$ Symmetry in $\alpha\text{-ZrCl}_3$ and Crystalline Spin-Orbital Liquids, *Phys. Rev. Lett.* **121**, 097201 (2018).
- [7] G. Khaliullin, Excitonic Magnetism in Van Vleck-type d^4 Mott Insulators, *Phys. Rev. Lett.* **111**, 197201 (2013).
- [8] O. N. Meetei, W. S. Cole, M. Randeria, and N. Trivedi, Novel magnetic state in d^4 Mott insulators, *Phys. Rev. B* **91**, 054412 (2015).
- [9] A. Jain, M. Krautloher, J. Porras, G. H. Ryu, D. P. Chen, D. L. Abernathy, J. T. Park, A. Ivanov, J. Chaloupka, G. Khaliullin *et al.*, Higgs mode and its decay in a two-dimensional antiferromagnet, *Nat. Phys.* **13**, 633 (2017).
- [10] S.-M. Souliou, J. Chaloupka, G. Khaliullin, G. Ryu, A. Jain, B. J. Kim, M. Le Tacon, and B. Keimer, Raman Scattering from Higgs Mode Oscillations in the Two-Dimensional Antiferromagnet Ca_2RuO_4 , *Phys. Rev. Lett.* **119**, 067201 (2017).
- [11] P. S. Anisimov, F. Aust, G. Khaliullin, and M. Daghofer, Nontrivial Triplon Topology and Triplon Liquid in Kitaev-Heisenberg-type Excitonic Magnets, *Phys. Rev. Lett.* **122**, 177201 (2019).
- [12] J. Chaloupka and G. Khaliullin, Highly frustrated magnetism in relativistic d^4 Mott insulators: Bosonic analog of the Kitaev honeycomb model, *Phys. Rev. B* **100**, 224413 (2019).
- [13] D. C. Wallace and T. M. McQueen, New honeycomb iridium(V) oxides: NaIrO_3 and $\text{Sr}_3\text{CaIr}_2\text{O}_9$, *Dalton Trans.* **44**, 20344 (2015).
- [14] M. Kusch, V. M. Katukuri, N. A. Bogdanov, B. Büchner, T. Dey, D. V. Efremov, J. E. Hamann-Borrero, B. H. Kim, M. Krisch, A. Maljuk *et al.*, Observation of heavy spin-orbit excitons propagating in a nonmagnetic background: the case of $(\text{Ba}, \text{Sr})_2\text{YIrO}_6$, *Phys. Rev. B* **97**, 064421 (2018).
- [15] Y. Miura, Y. Yasui, M. Sato, N. Igawa, and K. Kakurai, New-type phase transition of Li_2RuO_3 with honeycomb structure, *J. Phys. Soc. Jpn.* **76**, 033705 (2007).
- [16] Y. Miura, M. Sato, Y. Yamakawa, T. Habaguchi, and Y. Ōno, Structural Transition of Li_2RuO_3 induced by molecular-orbit formation, *J. Phys. Soc. Jpn.* **78**, 094706 (2009).
- [17] S. A. J. Kimber, C. D. Ling, D. J. P. Morris, A. Chemseddine, P. F. Henry, and D. N. Argyriou, Interlayer tuning of electronic

- and magnetic properties in honeycomb ordered $\text{Ag}_3\text{LiRu}_2\text{O}_6$, *J. Mater. Chem.* **20**, 8021 (2010).
- [18] R. Kumar, T. Dey, P. M. Ette, K. Ramesha, A. Chakraborty, I. Dasgupta, J. C. Orain, C. Baines, S. Tóth, A. Shahee *et al.*, Unconventional magnetism in the $4d^4$ -based $S = 1$ honeycomb system $\text{Ag}_3\text{LiRu}_2\text{O}_6$, *Phys. Rev. B* **99**, 054417 (2019).
- [19] S. Bette, T. Takayama, V. Duppel, A. Poulain, H. Takagi, and R. E. Dinnebier, Crystal structure and stacking faults in the layered honeycomb, delafossite-type materials $\text{Ag}_3\text{LiIr}_2\text{O}_6$ and $\text{Ag}_3\text{LiRu}_2\text{O}_6$, *Dalton Trans.* **48**, 9250 (2019).
- [20] F. L. Pratt, WIMDA: A muon data analysis program for the Windows PC, *Phys. B: Condens. Matter* **289-290**, 710 (2000).
- [21] N. Tateiwa, Y. Haga, Z. Fisk, and Y. Ōnuki, Miniature ceramic-anvil high-pressure cell for magnetic measurements in a commercial superconducting quantum interference device magnetometer, *Rev. Sci. Instrum.* **82**, 053906 (2011).
- [22] K. Kitagawa, H. Gotou, T. Yagi, A. Yamada, T. Matsumoto, Y. Uwatoko, and M. Takigawa, Space efficient opposed-anvil high-pressure cell and its application to optical and NMR measurements up to 9 GPa, *J. Phys. Soc. Jpn.* **79**, 024001 (2010).
- [23] C. L. Bull, N. P. Funnell, M. G. Tucker, S. Hull, D. J. Francis, and W. G. Marshall, PEARL: The high pressure neutron powder diffractometer at ISIS, *High Press. Res.* **36**, 493 (2016).
- [24] J. M. Besson, R. J. Nelmes, G. Hamel, J. S. Loveday, G. Weill, and S. Hull, Neutron powder diffraction above 10 GPa, *Phys. B: Condens. Matter* **180-181**, 907 (1992).
- [25] T. Irifune, A. Kurio, S. Sakamoto, T. Inoue, and H. Sumiya, Ultrahard polycrystalline diamond from graphite, *Nature (London)* **421**, 599 (2003).
- [26] N. Ishimatsu, K. Matsumoto, H. Maruyama, N. Kawamura, M. Mizumaki, H. Sumiya, and T. Irifune, Glitch-free x-ray absorption spectrum under high pressure obtained using nanopolycrystalline diamond anvils, *J. Synchrotron Radiat.* **19**, 768 (2012).
- [27] B. O. Roos, P. R. Taylor, and P. E. Sigbahn, A complete active space SCF method (CASCF) using a density matrix formulated super-CI approach, *Chem. Phys.* **48**, 157 (1980).
- [28] H. Werner and P. J. Knowles, An efficient internally contracted multiconfiguration-reference configuration interaction method, *J. Chem. Phys.* **89**, 5803 (1988).
- [29] N. A. Bogdanov, R. Maurice, I. Rousochatzakis, J. van den Brink, and L. Hozoi, Magnetic State of Pyrochlore $\text{Cd}_2\text{Os}_2\text{O}_7$ Emerging from Strong Competition of Ligand Distortions and Longer-Range Crystalline Anisotropy, *Phys. Rev. Lett.* **110**, 127206 (2013).
- [30] L. Hozoi, L. Siurakshina, P. Fulde, and J. van den Brink, *Ab initio* determination of Cu $3d$ orbital energies in layered copper oxides, *Sci. Rep.* **1**, 65 (2011).
- [31] K. A. Peterson, D. Figgen, M. Dolg, and H. Stoll, Energy-consistent relativistic pseudopotentials and correlation consistent basis sets for the $4d$ elements Y–Pd, *J. Chem. Phys.* **126**, 124101 (2007).
- [32] T. H. Dunning, Gaussian basis sets for use in correlated molecular calculations. I. The atoms boron through neon and hydrogen, *J. Chem. Phys.* **90**, 1007 (1989).
- [33] K. Pierloot, B. Dumez, P.-O. Widmark, and B. O. Roos, Density matrix averaged atomic natural orbital (ANO) basis sets for correlated molecular wave functions, *Theoret. Chim. Acta* **90**, 87 (1995).
- [34] P. Fuentealba, H. Preuss, H. Stoll, and L. Von Szentpaly, A proper account of core-polarization with pseudopotentials: single valence-electron alkali compounds, *Chem. Phys. Lett.* **89**, 418 (1982).
- [35] H. Stoll, P. Fuentealba, P. Schwerdtfeger, J. Flad, L. v. Szentpaly, and H. Preuss, Cu and Ag as one-valence-electron atoms: CI results and quadrupole corrections for Cu_2 , Ag_2 , CuH , and AgH , *J. Chem. Phys.* **81**, 2732 (1984).
- [36] J. Pipek and P. G. Mezey, A fast intrinsic localization procedure applicable for *ab initio* and semiempirical linear combination of atomic orbital Wave Functions, *J. Chem. Phys.* **90**, 4916 (1989).
- [37] A. Berning, M. Schweizer, H.-J. Werner, P. J. Knowles, and P. Palmieri, Spin-orbit matrix elements for internally contracted multireference configuration interaction wavefunctions, *Mol. Phys.* **98**, 1823 (2000).
- [38] H.-J. Werner, P. J. Knowles, F. R. Manby, J. A. Black, K. Doll, A. Heselmann, D. Kats, A. Kohn, T. Korona, D. A. Kreplin *et al.*, The MOLPRO quantum chemistry package, *J. Chem. Phys.* **152**, 144107 (2020).
- [39] V. Antonov, B. Harmon, and A. Yaresko, *Electronic Structure and Magneto-Optical Properties of Solids* (Kluwer Academic Publishers, Dordrecht, 2004).
- [40] F. Bahrami, E. M. Kenney, C. Wang, A. Berlie, O. I. Lebedev, M. J. Graf, and F. Tafti, Effect of structural disorder on the Kitaev magnet $\text{Ag}_3\text{LiIr}_2\text{O}_6$, *Phys. Rev. B* **103**, 094427 (2021).
- [41] W. C. Sheets, E. S. Stampler, M. I. Bertoni, M. Sasaki, T. J. Marks, T. O. Mason, and K. R. Poeppelmeier, Silver delafossite oxides, *Inorg. Chem.* **47**, 2696 (2008).
- [42] K. Momma and F. Izumi, VESTA3 for three-dimensional visualization of crystal, volumetric and morphology data, *J. Appl. Crystallogr.* **44**, 1272 (2011).
- [43] See Supplemental Material at <http://link.aps.org/supplemental/10.1103/PhysRevResearch.4.043079> for supplemental figures and tables and the discussion about the J -dimer model and it includes Refs. [57–62].
- [44] Y. Takikawa, S. Ebisu, and S. Nagata, Van Vleck paramagnetism of the trivalent Eu ions, *J. Phys. Chem. Solids* **71**, 1592 (2010).
- [45] H. Takahashi, H. Suzuki, J. Bertinshaw, S. Bette, C. Mühle, J. Nuss, R. Dinnebier, A. Yaresko, G. Khaliullin, H. Gretarsson *et al.*, Nonmagnetic $J = 0$ State and Spin-Orbit Excitations in K_2RuCl_6 , *Phys. Rev. Lett.* **127**, 227201 (2021).
- [46] I. Y. Arapova, A. L. Buzlukov, A. Y. Germov, K. N. Mikhalev, T.-Y. Tan, J.-G. Park, and S. V. Streltsov, Magnetic properties of Li_2RuO_3 as studied by NMR and LDA + DMFT calculations, *JETP Lett.* **105**, 375 (2017).
- [47] S. A. J. Kimber, I. I. Mazin, J. Shen, H. O. Jeschke, S. V. Streltsov, D. N. Argyriou, R. Valentí, and D. I. Khomskii, Valence bond liquid phase in the honeycomb lattice material Li_2RuO_3 , *Phys. Rev. B* **89**, 081408(R) (2014).
- [48] V. Hermann, M. Altmeyer, J. Ebad-Allah, F. Freund, A. Jesche, A. A. Tsirlin, M. Hanfland, P. Gegenwart, I. I. Mazin, D. I. Khomskii *et al.*, Competition between spin-orbit coupling, magnetism, and dimerization in the honeycomb iridates: α - Li_2IrO_3 under pressure, *Phys. Rev. B* **97**, 020104(R) (2018).
- [49] T. Takayama, A. Krajewska, A. S. Gibbs, A. N. Yaresko, H. Ishii, H. Yamaoka, K. Ishii, N. Hiraoka, N. P. Funnell, C. L. Bull *et al.*, Pressure-induced collapse of the spin-orbital Mott state in the hyperhoneycomb iridate β - Li_2IrO_3 , *Phys. Rev. B* **99**, 125127 (2019).

- [50] T. Biesner, S. Biswas, W. Li, Y. Saito, A. Pustogow, M. Altmeyer, A. U. B. Wolter, B. Büchner, M. Roslova, T. Doert *et al.*, Detuning the honeycomb of α -RuCl₃: pressure-dependent optical studies reveal broken symmetry, *Phys. Rev. B* **97**, 220401(R) (2018).
- [51] S. Yun, K. H. Lee, S. Y. Park, T.-Y. Tan, J. Park, S. Kang, D. I. Khomskii, Y. Jo, and J.-G. Park, Magnetic and electrical anisotropy with correlation and orbital effects in dimerized honeycomb ruthenate Li₂RuO₃, *Phys. Rev. B* **100**, 165119 (2019).
- [52] H. Liu and G. Khaliullin, Pseudo-Jahn-Teller Effect and Magnetoelastic Coupling in Spin-Orbit Mott Insulators, *Phys. Rev. Lett.* **122**, 057203 (2019).
- [53] G. Fabbri, A. Thorn, W. Bi, M. Abramchuk, F. Bahrami, J. H. Kim, T. Shinmei, T. Irifune, F. Tafti, A. N. Kolmogorov *et al.*, Complex pressure-temperature structural phase diagram of the honeycomb iridate Cu₂IrO₃, *Phys. Rev. B* **104**, 014102 (2021).
- [54] T. Takayama, A. Krajewska, A. Gibbs, C. Bull, M. Blankenhorn, G. McNally, and H. Takagi, STFC ISIS Neutron and Muon Source (2019), <https://doi.org/10.5286/ISIS.E.RB1920241>.
- [55] J. Bertinshaw, T. Takayama, B.-J. Kim, R. Bewley, H. Takagi, and B. Keimer, STFC ISIS Neutron and Muon Source (2018), <https://doi.org/10.5286/ISIS.E.RB1820520>.
- [56] T. Takayama, D. P. Sari, I. Watanabe, M. Blankenhorn, A. Krajewska, H. Rozak, and H. Takagi, STFC ISIS Neutron and Muon Source (2019), <https://doi.org/10.5286/ISIS.E.RB1970001>.
- [57] J. Park, T.-Y. Tan, D. T. Adroja, A. Daoud-Aladine, S. Choi, D.-Y. Cho, S.-H. Lee, J. Kim, H. Sim, T. Morioka *et al.*, Robust singlet dimers with fragile ordering in two-dimensional honeycomb lattice of Li₂RuO₃, *Sci. Rep.* **6**, 25238 (2016).
- [58] M. P. Jimenez-Segura, A. Ikeda, S. A. J. Kimber, C. Giacobbe, S. Yonezawa, and Y. Maeno, Effect of delithiation on the dimer transition of the honeycomb-lattice ruthenate Li_{2-x}RuO₃, *Phys. Rev. B* **94**, 115163 (2016).
- [59] M. T. F. Telling, K. S. Knight, F. L. Pratt, A. J. Church, P. P. Deen, K. J. Ellis, I. Watanabe, and R. Cywinski, Pressure-dependent spin fluctuations and magnetic structure in the topologically frustrated spin glass alloy Y(Mn_{0.95}Al_{0.05})₂, *Phys. Rev. B* **85**, 184416 (2012).
- [60] D. L. Decker, High-pressure equation of state for NaCl, KCl, and CsCl, *J. Appl. Phys.* **42**, 3239 (1971).
- [61] A. C. Larson and R. B. Von Dreele, General Structure Analysis System (GSAS), Report No. LAUR 86-748, Los Alamos National Laboratory (2000).
- [62] B. H. Toby and R. B. Von Dreele, GSAS-II: The genesis of a modern open-source all purpose crystallography software package, *J. Appl. Crystallogr.* **46**, 544 (2013).